SECTION 1
PHYSICS OF RADIATION DAMAGES AND EFFECTS IN SOLIDS

https://doi.org/10.46813/2024-152-003

UDC 669.017:539.16

HARDENING BEHAVIOR OF NUCLEAR STRUCTURAL MATERIALS UNDER ION IRRADIATION

S.O. Karpov, M.O. Azarenkov, G.D. Tolstolutska
National Science Center "Kharkov Institute of Physics and Technology", Kharkiv, Ukraine
E-mail: karpofff@kipt.kharkov.ua

The evaluation of irradiation hardening and embrittlement is critically important for the development of next-generation nuclear structural materials tolerant to neutron irradiation. This review summarizes research progress on experimental observations aimed at elucidating the mechanisms of radiation-induced hardening in ion-irradiated materials, focusing on the correlation between irradiation effects and mechanical property changes. We present the basic information for the application of ion irradiation and nanoindentation techniques to characterize the mechanical properties of nuclear structural materials. The effects of irradiation on advanced structural materials, including oxide dispersion strengthened (ODS) austenitic steels, ferritic-martensitic steels, and high-entropy alloys, are analyzed. The dependence of hardening parameters on the irradiation dose and their relationship with microstructural evolution are examined. Findings indicate that these advanced alloys exhibit reduced susceptibility to irradiation-induced hardening compared to conventional austenitic stainless steels.

INTRODUCTION

The longevity of structural materials used in the current fleet of water-cooled reactors, as well as in advanced fission and future fusion reactors, is hindered by radiation-induced degradation. The operating conditions of these materials, including high temperatures and corrosive coolants, further exacerbate this issue [1, 2]. To address this challenge, predicting the response of materials to high levels of irradiation damage is crucial for both the life extension of current reactors and the development of next-generation reactors. Fig. 1 illustrates the temperature and dose ranges for a variety of nuclear reactors. In comparison to current water-cooled reactors, all advanced reactor designs are intended to operate at elevated temperatures and significantly higher levels of radiation exposure.

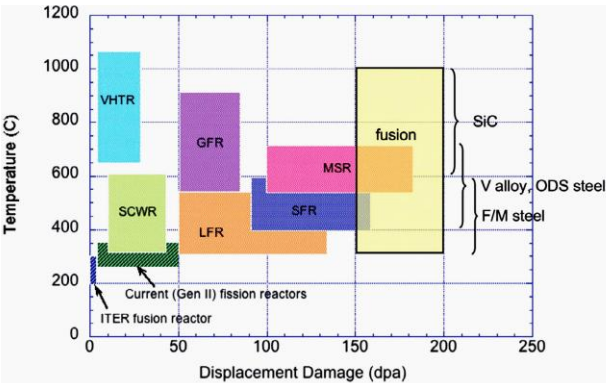

Fig. 1. Temperature and dose ranges for various nuclear reactors [2]

Understanding the evolution of microstructure and microstructure-related degradation mechanisms is essential for ensuring reliable performance of materials at high displacements per atom (dpa) and temperatures. This knowledge is critical for mitigating the detrimental effects of radiation-induced damage on structural materials, thereby ensuring the safe and efficient operation of nuclear reactors.

During the long-term operation of nuclear reactors, high-energy neutron irradiation results in atomic-level changes in the crystalline structure, with the nucleation of defects such as dislocation loops, stacking faults, bubbles, and voids. These defects significantly impair the physical properties of reactor materials, leading to issues such as swelling, irradiation hardening, embrittlement, and irradiation creep [3]. Irradiation hardening is a critical phenomenon observed in nuclear structural materials that increases the yield strength of the material, but simultaneously reduces the ductility and causes embrittlement.

Ion irradiation is a commonly employed technique for simulating neutron damage under reactor conditions. Among the various methods utilized to study the irradiation hardening phenomenon, ion irradiation possesses a number of inherent advantages. These advantages include the availability of sufficient irradiation sources, the absence of induced radioactivity, shorter experimental periods, and reduced costs. Despite these advantages, ion irradiation is not a perfect substitute for neutron irradiation. The primary limitation is that the damage induced by ions is typically confined to a shallow surface layer, which complicates the application of conventional mechanical testing. Consequently, small-scale test techniques with high spatial resolution, such as nanoindentation (NI), are required to characterize the localized mechanical properties of ion-irradiated materials. NI offers the benefits of easy experimental preparation and the ability to generate statistically rich datasets, making it a valuable tool in assessing the mechanical degradation of ion-irradiated materials.

Ion irradiation in conjunction with nanoindentation has been extensively employed in the examination of various nuclear structural materials, including pure metals and alloys [4–6]. Furthermore, a combination of experimental techniques, numerical simulations, and theoretical modeling has facilitated the identification of irradiation-induced defects and the characterization of microstructure evolution within the plastic zone, thereby providing a deeper understanding of the fundamental mechanisms of hardening and embrittlement.

The phenomenon of irradiation-induced hardening and embrittlement has been the subject of extensive investigation in various nuclear structural materials exhibiting distinct crystalline structures, including face-centered cubic (FCC), body-centered cubic (BCC), and hexagonal close-packed (HCP) materials. Of particular significance is that austenitic steels, ferritic-martensitic steels, and high-entropy alloys (HEAs) have been the subject of interest due to their unique properties and responses to irradiation, which make their comprehensive study essential for advanced nuclear applications.

Austenitic steels, known for their excellent corrosion resistance and high-temperature properties, are widely used in nuclear power engineering. However, their relatively lower radiation resistance poses a challenge. Enhancing their radiation tolerance by introducing nano-sized oxide precipitates can impede dislocation motion and maintain high tensile and creep strength, crucial for sustaining structural integrity under irradiation.

Ferritic-martensitic (F-M) steels are prime candidates for high-dose nuclear applications due to their higher resistance to neutron irradiation compared to austenitic steels. These steels exhibit advantageous properties such as higher thermal conductivity, lower coefficients of thermal expansion, good creep characteristics, and high strength at elevated temperatures. The radiation-induced hardening and embrittlement in these steels necessitate a deep understanding of their microstructural evolution to mitigate mechanical property degradation and ensure long-term performance.

High-entropy alloys, a novel class of materials, offer promising characteristics such as high strength, corrosion resistance, and thermal stability due to their unique multicomponent composition. Recent studies indicate that certain HEAs demonstrate superior resistance to irradiation, including reduced swelling and damage accumulation, making them promising candidates for high-temperature nuclear structural applications. Studying these materials is essential for developing robust nuclear structural components that can withstand the extreme conditions of irradiation, thereby enhancing the safety and efficiency of current and future nuclear reactors.

To enhance understanding of the mechanisms governing radiation-induced hardening in ion-irradiated materials, this paper provides a concise overview of research findings, encompassing both experimental observations and some theoretical models.

The main contents are organized as follows: in Section 1, the general interpretation of nanohardness data is outlined. In Section 2, radiation effects in nuclear structural materials are discussed. Sections 3 addresses the dose and temperature dependences of irradiation hardening. The subsequent section provides a detailed analysis of the irradiation hardening behavior of selected structural alloys. Finally, concluding remarks are made in Summary section.

1. INTERPRETATION OF HARDNESS DATA OBTAINED BY NANOINDENTATION TECHNIQUE

Nanoindentation techniques have gained considerable popularity in recent years due to their versatility and ability to address various physical problems. As a leading testing methodology, nanoindentation is particularly well-suited for elucidating the fundamental laws governing the behavior of nanometer-scale surface layers and submicron volumes of diverse materials.

The operational mode of nanoindenters involves the penetration of a geometrically certified indenter under the influence of a prescribed normal force profile P(t) and simultaneous registration of the depth of penetration h(t) into the material. One of the attractive features of nanoindentation is its ability to provide various quantitative characteristics of materials, such as Young's modulus, hardness, fracture toughness, etc. [7]. However, the interpretation of experimental data obtained through nanoindentation is a complex task, as the measured properties at a given indentation depth h represent an average mechanical response of the plastic zone, which encompasses not only heterogeneously distributed microstructures induced by ion irradiation but also length-scale (and other) effects introduced by the nanoindentation process itself [8, 9]. Generally, the indentation hardness of ion-irradiated materials is a superposition of bulk hardness, indentation size effect, and irradiation-induced hardening [10, 11].

1.1. THE INDENTATION SIZE EFFECT

The Indentation Size Effect (ISE) denotes the phenomenon where hardness exhibits a dependency on indentation depth, characterized by an increase in hardness with decreasing penetration depth, particularly in the shallow range of indentation depths [12–15]. This phenomenon has been widely observed across a broad range of materials. The most widely accepted and pioneering model for ISE, developed by Nix and Gao (Equation (1)) [16], is grounded in the concept of strain gradient plasticity [17, 18] and geometrically necessary dislocations (GNDs). GNDs are dislocations that exceed statistically stored dislocations (SSDs) in number. GNDs are necessary to accommodate material deformation caused by the indenter after indentation. As a result, ISE is observed at small indentation depths, where the availability of SSDs is limited, necessitating the introduction of GNDs to facilitate permanent shape change [19].

$$\frac{H}{H_0} = \sqrt{1+\frac{h^*}{h}}, \qquad (1)$$

where H is the hardness measured at a depth h; H_0 is the hardness at the infinite depth (i.e., the macroscopic hardness), and h* is a characteristic length depending on the properties of a material and the indenter tip shape.

The plastic deformation zone beneath the indenter extends significantly deeper into the material than the displacement of the indenter itself (Fig. 2).

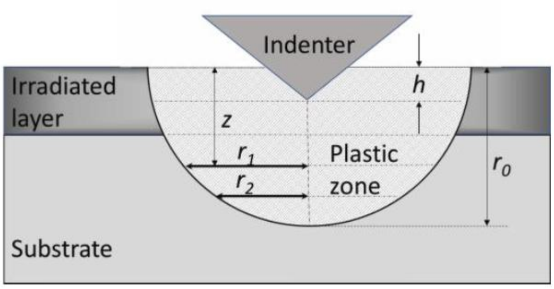

Fig. 2. Schematic of the indentation test. The indentation-induced plastic zone is assumed to be a hemisphere

Previous studies have indicated that the plastic zone can be approximated by a hemisphere with a radius of 5 to 10 times the indentation depth [20]. Consequently, in irradiated materials with a shallow damage depth, part of the plastic zone extends into the underlying, unirradiated material (soft substrate). As the indentation depth increases, the measured hardness approaches that of the unirradiated material, since the proportion of unirradiated material within the plastic zone increases. The transition point between these areas defines the critical indentation depth, h_c.

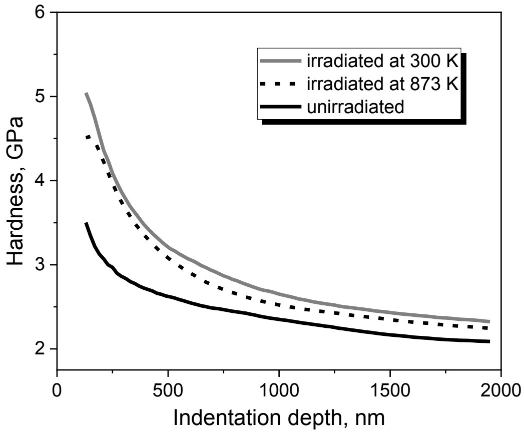

a

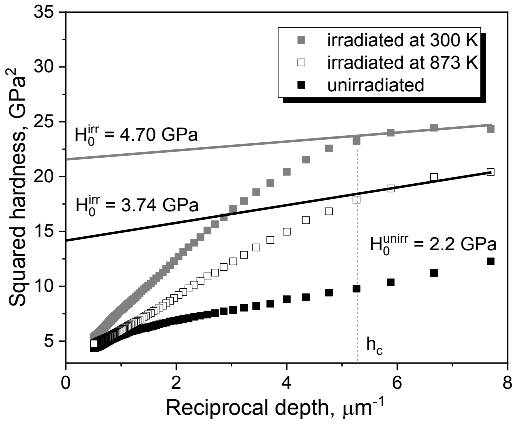

b

Fig. 3. The experimental profiles of nanoindentation hardness vs. indentation depth measured for the unirradiated and irradiated to a dose of 50 dpa 18Cr10NiTi steel (a); Nix-Gao plot for unirradiated and argon irradiated steel (b)

Kasada et al. first proposed the method for considering the soft substrate effect for materials irradiated with accelerated ions [21], identifying such materials as systems with coatings or as "hardened layer–substrate" systems. According to Kasada, the bulk equivalent hardness, H_0, of the ion-irradiated region can be determined by least square fitting of the hardness data up to the critical depth h_c. By redrawing the experimental profiles of hardness (Fig. 3) in the coordinates "squared hardness – reciprocal depth", the bulk-equivalent hardness of the ion-irradiated region can be evaluated from the intercept of the linear fitting of data in the region when $h < h_c$.

1.2. THE VOLUME FRACTION MODEL

The values of bulk-equivalent hardness discussed in previous paragraphs have been evaluated in accordance with the methodology of Kasada et al. [21] from the data fitting of the Nix-Gao plot. In the case of ion-irradiated materials, the volume encompassed by the plastic zone often exhibits pronounced damage gradients. The typical damage profile resulting from single-ion irradiation of metallic materials is shown in Fig. 4.

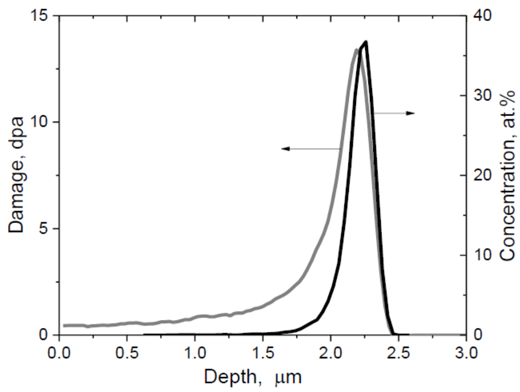

Fig. 4. Calculated damage profile resulting from high-energy He-ion irradiation of SS316 steel

However, Kasada's method did not take into account the damage gradient effect (DGE). To extract irradiation induced hardening effect precisely with a consideration of DGE, a rule-of-mixtures type volume fraction approach can be used. This method has recently been described in [10, 11, 22].

In the framework of this approach, the hardness is calculated as a volume-weighted average of the hardness of plastically deformed material in the irradiated layer and the unirradiated underlying substrate. The model assumes a hemispherical plastic zone beneath the surface, divided into segments with dose-dependent hardness (see Fig. 2). The volume of each segment is calculated, and its radiation-induced hardening is determined using a power law relationship. The detailed description of simulation can be found in [11]. The overall hardness at each indent depth is the weighted average of the segment hardness values. The method allows to distinguish the contribution of radiation hardening, ISE and bulk-equivalent hardness to the measured hardness. Fig. 5 shows an example of hardness-depth curve simulations as well as experimental data for the case of helium irradiation of SS316 steel [11].

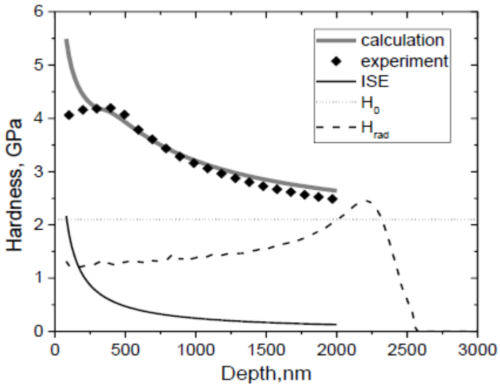

Fig. 5. Experimental hardness vs. displacement plot for 1.4 MeV He ions. The bold solid grey line shows the hardness obtained from the volume fraction model. The dotted lines show the material hardness at an infinite depth, H_0; fine black lines – H_{ISE} vs. indenter displacement. The dashed line shows the irradiation-induced hardness H_{rad} vs. depth

The results show strong correlation with experimental data, effectively simulating hardness variations with depth and distinguishing between radiation hardening, ISE, and the bulk equivalent hardness.

1.3. INDENTATION PILE-UP OR SINK-IN

An essential characteristic of indentation experiments is that the material around the contact area tends to deform upwards (pile-up) or downwards (sink-in) with respect to the indented surface plane [23, 24]. This deformation behavior depends on the strain-hardening properties of the material under examination. When a sample is fully annealed and possesses high strain-hardening potential, the area around indents tends to sink in. Conversely, the surface around indents tends to pile up when the indented sample is heavily pre-strained or exhibits low strain-hardening potential.

The pile-up/sink-in behavior exhibited during deformation can result in distortion of the contact area, which may lead to an overestimation or underestimation of the indentation hardness. Recently, various methods for pile-up corrected hardness have been proposed. Hardie et al. [25] introduced an approach based on the actual contact area measured by scanning electron microscopy (SEM). Pile-up correction (PUC) can then be performed using the ratio of the actual contact area to the pile-up unaffected area. Heintze et al. [26] proposed the elastic-modulus-based correction (EMC) method to correct nanoindentation hardness data. This method utilizes the square function of the indentation modulus to the elastic modulus for correcting indentation hardness, with the advantage of not requiring additional measurements. Another method, proposed in [27], corrects nanoindentation hardness using the difference in the actual elastic modulus between the ion-irradiated damaged layer and the unirradiated material. However, this method requires additional transient grating laser measurements.

Fig. 6 illustrates the approach proposed in [28] and applied in nanoindentation studies of T91 steel using a Berkovich indenter [29]. Following the indentation process, the resulting impressions were imaged using scanning electron microscopy in order to measure the contact areas and examine the extent of pile-up. Two different contact areas were determined from the SEM images. The pile-up unaffected corner-to-corner area (A_{cc}) represents the area of the triangle defined by the corners of the hardness impression (see Fig. 6,b,e). The actual contact area (A_{act}), which includes the extra area contained in the pile-up, was also measured (see Fig. 6,c,f). These specified areas were determined by digital image processing, and their ratio, A_{act}/A_{cc}, provided an estimation of the pile-up extent.

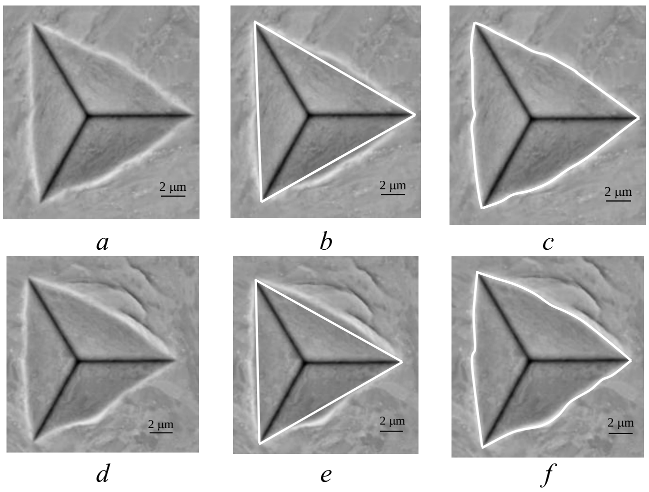

Fig. 6. SEM images showing deformed regions surrounding indents in un-irradiated (a, b, c) and irradiated (d, e, f) regions. Corner-to-corner (A_{cc}) of contact area (b, e) and actual (A_{act}) contact area (c, f) are shown

The values of the correction factor, A_{act}/A_{cc}, ranged from 1.10 to 1.18 and exhibited statistical scatter for both as-received and irradiated specimens. Notably, the average value of 1.14 ± 0.04 correlates well with the EMC factor according to Heintze's approach for the same steel [26].

Depending on the direction of indentation relative to the irradiation direction, nanoindentation of ion-irradiated materials can be classified into surface NI and cross-sectional NI. Surface NI, where the indentation direction is parallel to the irradiation direction, has been extensively studied and remains the most commonly applied method. This approach necessitates the simultaneous consideration of defect gradient distribution, indentation size effect, and the influence of the unirradiated soft substrate. In contrast, cross-sectional NI, where the indentation direction is perpendicular to the irradiation direction, provides an effective means to avoid the ISE by comparing hardness (H) variations at the same indentation depth (h) along the irradiation direction.

2. RADIATION DEFECTS CONTRIBUTING TO HARDENING

For over half a century, a comprehensive understanding of the phenomenon of radiation damage to materials under irradiation has been established. Radiation-induced damage is a significant concern for reactor structural materials, as high-energy particles can displace lattice atoms from their original sites, which subsequently interact with the surrounding matrix forming a collision cascade. Following cooling, a portion of the resulting point defects, such as interstitials and vacancies, recombine; however, the concentration of remaining point defects significantly exceeds equilibrium levels. This drives the material system into thermodynamic nonequilibrium, resulting in various modifications to the microstructure. Dislocation loops form due to the collapse of the interstitial-rich cascade shell, while the accumulation of vacancies leads to void nucleation. Preferential coupling between alloying elements and defect fluxes causes elemental segregation at defect sinks, and the stability of precipitates is significantly affected by displacement cascades and radiation-enhanced diffusion. Upon plastic deformation, these nano-scale defects serve as obstacles that impede the movement of sliding dislocations, subsequently affecting the mechanical behavior of irradiated metals [30, 31]. The cumulative effect of these radiation-induced defects and microstructural changes can significantly degrade the integrity of reactor structural materials, emphasizing the need for thorough understanding and development mitigation strategies to ensure safe and reliable operation of nuclear reactors.

2.1. EFFECT OF DISLOCATION LOOPS IN AUSTENITIC ALLOYS

The irradiation of austenitic steels at temperatures below approximately 0.35 T_M results in the formation of high-density ensemble of clustered defects, which significantly contribute to hardening [32]. The defect population is predominantly composed of two distinct types: small black-dot defects with a size of approximately 2 nm, and larger Frank faulted loops. Frank loops are characterized by habit planes of {111} and Burgers vectors of the 1/3<111> type. Notably, the prevalence of black-dots increases with low-temperature irradiation conditions.

TEM micrographs in Fig. 7 show the microstructural evolution of SS316 irradiated with 1.4 MeV argon ions at room temperature to 0.5 and 3 dpa. All images were recorded under bright-field down-zone imaging conditions at [011] axis zone [33].

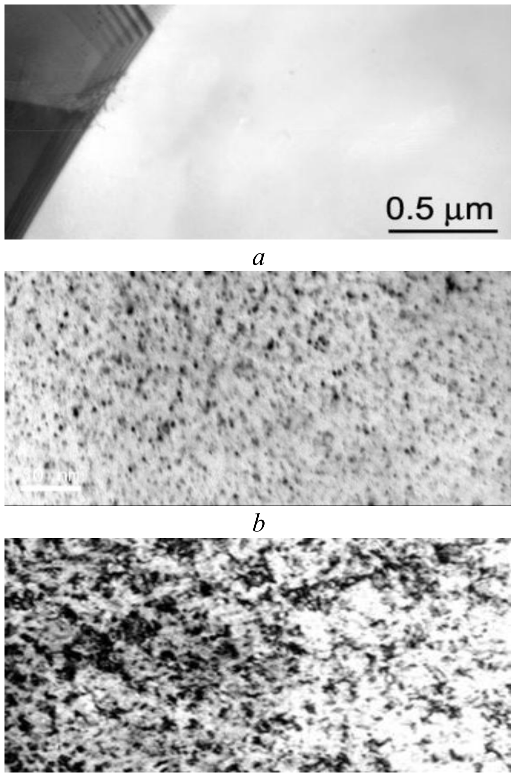

Fig. 7. Initial microstructure of SS316 (a) and irradiated at T_{room} with 1.4 MeV Ar ions to 0.5 (b) and 3 dpa (c)

Irradiated samples showed significant changes in the microstructure as compared to the unirradiated sample. The main irradiation defects observed were defect clusters at low doses and dislocation loops at higher doses. Tilting experiments clearly showed the dislocation nature of observed defects. Pre-existing dislocations were dissolved and uniform network dislocations formed at 3.0 dpa. The microstructure was basically unchanged from 3.0 to 5.0 dpa. The final microstructure is consist of uniform network dislocations and black-dots.

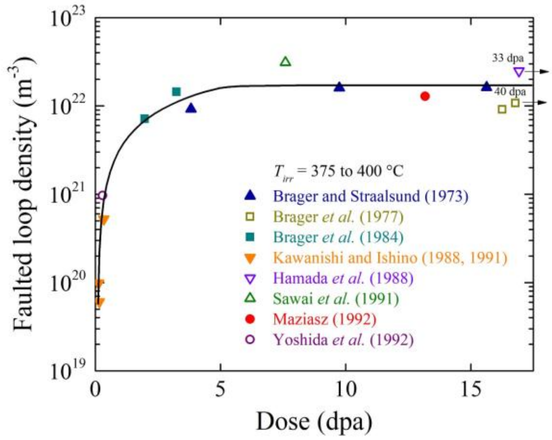

Fig. 8. A graphical representation of the dose-dependent variation in faulted loop density in neutron-irradiated SA austenitic stainless steels, as originally reported in [34, 37]. The original data underlying this graph were obtained from sources [35, 36, 38, 39, 40–44]

Numerous studies have previously investigated the formation of Frank faulted loops in austenitic stainless steels irradiated with neutrons. Fig. 8 illustrates the dose-dependent behavior of Frank loop density in austenitic stainless steels irradiated at approximately 400 °C. The results demonstrate that the Frank loop density reaches saturation after approximately 3 dpa of neutron irradiation.

Furthermore, the density of Frank loops is also found to be significantly influenced by the irradiation temperature. Fig. 9 illustrates the temperature-dependent variation in Frank loop density in high-dose (>10 dpa) neutron-irradiated austenitic stainless steel 316. Notably, as depicted in this figure, the Frank loop density exhibits a steep decline with increasing temperature above 300 °C.

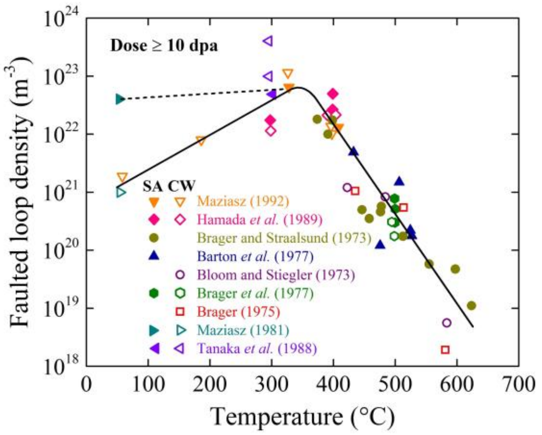

Fig. 9. The temperature-dependent behavior of faulted loop density in neutron-irradiated type 316 austenitic stainless steel, as previously reported in [34, 37]. The underlying data are derived from [35, 36, 38, 39, 45–50]

At intermediate temperatures, void swelling emerges as a significant radiation-induced concern for austenitic stainless steels, particularly at high doses, posing a critical challenge to the structural integrity and performance of these materials. In addition to void swelling, radiation-induced segregation and precipitation phenomena are also observed at intermediate temperatures. Particularly, Ni_3Si (γ′) has been identified as a radiation-induced phase that forms in neutron-irradiated austenitic stainless steel 316, as reported by previous studies [51–53].

2.2. EFFECT OF DISLOCATION LOOPS IN FERRITIC-MARTENSITIC ALLOYS

In the case of high-chromium ferritic-martensitic steels, the most significant radiation effect is the deterioration of mechanical properties due to irradiation hardening and embrittlement at low temperatures. This phenomenon is attributed to radiation-induced microstructural modifications, including the accumulation of dislocation loops and the precipitation of new phases [54, 55].

Transmission electron microscopy studies of F-M alloys irradiated at various doses have revealed that irradiation-induced dislocation loops begin to emerge at approximately 1 dpa and exhibit a significant increase in density by 1–2 orders of magnitude between 1 and 3 dpa. It was demonstrated that dislocation loops induced by both ion and neutron irradiations in α-iron, Fe-Cr model alloys, and F-M steels exhibit a_0<100> or a_0/2<111> crystallographic orientation. The stability of a_0/2<111> loops relative to a_0<100> loops is significantly influenced by the irradiation temperature [56]. Mobile a_0/2<111> loops are generated at lower temperatures and tend to decorate pre-existing dislocations. In contrast, the prevalence of sessile a_0<100> loops is greater at higher temperatures, exhibiting a more uniform spatial distribution.

2.3. BUBBLES AND VOIDS

Microstructural observations reveal that in the irradiated layer, besides interstitial loops, nano-sized voids may also be present, which are believed to contribute to radiation hardening [57]. Furthermore, atomic-scale modeling was employed [58] to investigate the interaction between edge dislocations and voids in FCC-copper and BCC-iron. Voids with diameters ranging from 6 to 8 nm were examined at temperatures between 0 and 600 K, under various strain rates. The results demonstrate that voids in iron act as significant obstacles to dislocation motion, whereas small voids in copper are found to be significantly weaker obstacles compared to those in iron. Large voids in copper are at least as strong obstacles as those in iron, with the underlying mechanism dependent on temperature.

Gas implantation, especially noble gas implantation, can promote the creation of various types of defect clusters [59, 60]. For instance, in various structural steels after He irradiation, both accumulations of defects and helium bubbles are observed, the size of which increases with increasing irradiation dose, and the change in the density of defects depends on the irradiation temperature.

In particular, experimental evidence from a nanoindentation study on He-irradiated stainless steel 316 has demonstrated that dislocation sliding is impeded due to the presence of dislocation loops [61]. Conversely, irradiation-induced bubbles have been found to present relatively weak obstacles compared to dislocation loops, as the distance between pinning points is significantly greater than that between bubbles (Fig. 10). Therefore, according to the authors [61], the contribution of nanosized bubbles to radiation hardening can be neglected when considering He-implanted materials.

In contrast, radiation-induced gas-filled nanocavities have been demonstrated to contribute to an increase in hardness in 18Cr10NiTi and 18Cr10NiTi-ODS alloys following Ar^+ ion irradiation. Moreover, Ar-filled nanocavities exhibit a clear tendency to enhance barrier strength with decreasing cavity size (Fig. 11) [62].

Furthermore, according to [63], the impeding effect of gas bubbles on sliding dislocations depends on the gas atom/vacancy ratio. Molecular dynamics simulations have elucidated the interaction between an edge dislocation and a 2-nm void or He bubble in iron single crystals, revealing that dislocations are significantly pinned by these defects. Notably, a 2-nm void serves as a more strong obstacle than a 2-nm He bubble at low He concentrations; however, at high He contents (five He atoms per vacancy), the He bubble proves to be a more effective barrier than the void. Thus, the role of these microscale defects as barriers to dislocation glide during plastic deformation, and their subsequent impact on the mechanical properties of irradiated metals, remains a topic of debate.

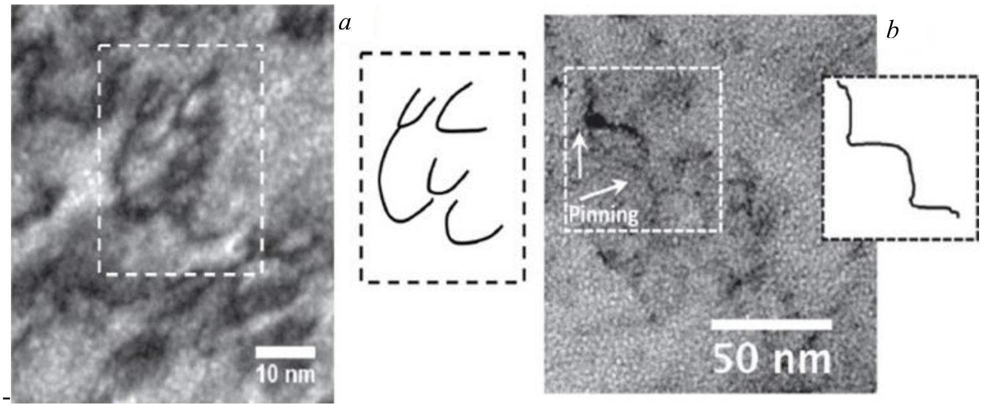

Fig. 10. TEM micrographs of 316 stainless steel subjected to Ar and He ion irradiation. Dislocations are (a) curved and (b) pinned by irradiation-induced defect clusters, and the pinning points are much farther apart than the bubbles (visible as white dots here) [61]

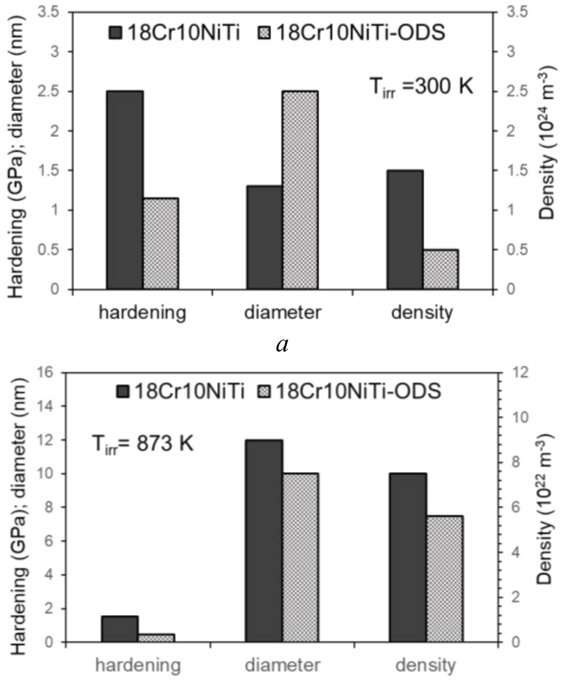

Fig. 11. The hardening of 18Cr10NiTi and 18Cr10NiTi-ODS steels and diameter and density of argon bubbles after irradiation to 50 dpa at T_{room} (a) and 873 K (b)

3. THE DOSE AND TEMPERATURE DEPENDENCES OF IRRADIATION HARDENING

As discussed in the previous section, an increase in the irradiation dose generally results in an increase in the number of point defects generated during collision cascades. This, in turn, leads to an increase in the density of defect clusters and dislocation loops that are observed in irradiated steels and model alloys. Cluster dynamics modeling [64] indicates that nanoscale dislocation loops can form from displacement cascades under reactor irradiation at neutron fluences as low as ~ 0.001 dpa, which is long before they can be detected by transmission electron microscopy. Nevertheless these unresolved by TEM defects have the potential to considerably impact on the hardness of irradiated material.

Figs. 12 and 13 represents the results of study of irradiation effect with 1.4 MeV argon ions within the range of doses 0…10 dpa at 300 K on the hardening of SS316 stainless steel [65]. As compared with the initial material, the specimens irradiated with argon ions show the increment of 1…2 GPa in hardness in the dose interval 0.1…10 dpa, which reveals the radiation-induced hardening of the steel. The hardness maximum was recorded at depths of 100…150 nm with its subsequent monotonic decrease, as the indentation depth increases (see Fig. 12).

The bulk-equivalent hardness (see Fig. 13) of the ion-irradiated region was evaluated using the methodology outlined by Kasada [21]. The findings indicate that the most pronounced effects are observed at low irradiation doses, with a transition to a quasi-saturated regime at high fluences.

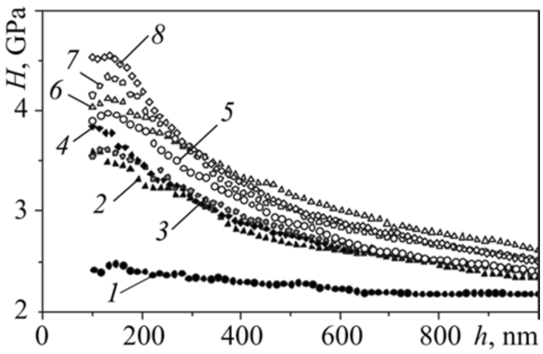

Fig. 12. Depth profiles of the nanohardness of SS316 steal after the irradiation with Ar + ions up to doses (dpa): 1 – 0; 2 – 0.1; 3 – 0.5; 4 – 0.7; 5 – 1; 6 – 2; 7 – 5; 8 – 10

Specifically, at a fluence of 0.5 dpa, the hardness exhibits a significant increase of approximately 1.3 GPa, representing a relative change of more than 50%. A damaging dose of 10 dpa yields a hardening effect of approximately 75%.

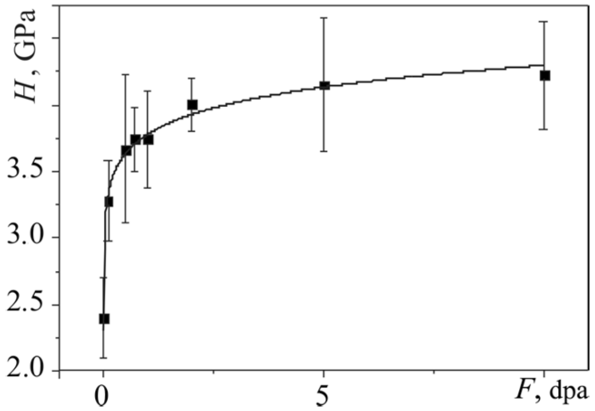

Fig. 13. Dependence of nanohardness on the dose of radiation at room temperature

TEM analysis of the irradiated samples revealed the formation of dislocation loops with approximately the same density across all irradiation doses at room temperature [65]. The microstructural evolution proceeds from isolated "black dots" to loops with diameters of approximately 15 nm and ultimately to a complex structure resulting from the entwining of dislocations. These results indicate that the largest relative increase in nanohardness is attributed to the formation of small defect clusters. In the course of their further evolution into loops and "tangles" of dislocations, this effect becomes weaker.

Considerable research has been devoted to elucidating the irradiation hardening behavior of metals, with a focus on correlating the change in strength with the number density and size of radiation-induced defects and irradiation dose. While different theories exist about the mechanisms behind irradiation hardening [66], models based on barrier hardening theory [67] have been widely used to understand the dose-dependent increase in yield stress.

In the regression analysis [66], the radiation-induced increase in yield stress was expressed by a power law equation: $\Delta\sigma_{ys} = h\cdot(dpa)^n$, where h and n are regression coefficients. The log-log plots of the data showed two distinct regimes: a low-dose regime where a hardening occurs and a high-dose regime where the log-log plot shows a considerably reduced slope. The average value of the exponent n was found to be: 0.5 for the low-dose regime, and 0.12 for the high-dose regime.

The log-log plot of the dose dependence of irradiation hardening in SS316 irradiated with 1.4 MeV Ar ions is presented in Fig. 14. Irradiation hardening is denoted as $\Delta H = H_0^{irr} - H_0^{as-recieved}$. The power-law approximation of hardening values was found to provide a satisfactory agreement with experimental data, with determined values of n equal to 0.47 and 0.13 for the low-dose and high-dose hardening regimes, respectively [11].

A comprehensive analysis of the n values in the low-dose regime revealed a range of 0.31–0.48 for a variety of FCC metals, whereas in the high-dose regime, the range was 0.01–0.24. Notably, the average n value for FCC metals in the low-dose regime was found to be slightly lower than that for BCC metals, with values of 0.4 and 0.55, respectively [20].

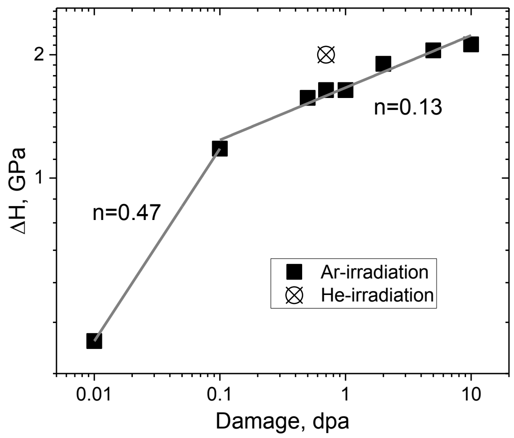

Fig. 14. Log-log plot for dose dependence of irradiation hardening of 316 stainless steels [11]

It is noteworthy that the radiation-induced hardening behavior discussed herein is characteristic not only for model alloys and widely used commercial steels but is also observed in a range of advanced alloys with potential applications in nuclear materials science. As illustrated in Fig. 15, the dose-dependence of radiation hardening for multicomponent concentrated alloys demonstrates the most pronounced effects of irradiation at low doses, transitioning to a quasi-saturated regime at higher fluences [68].

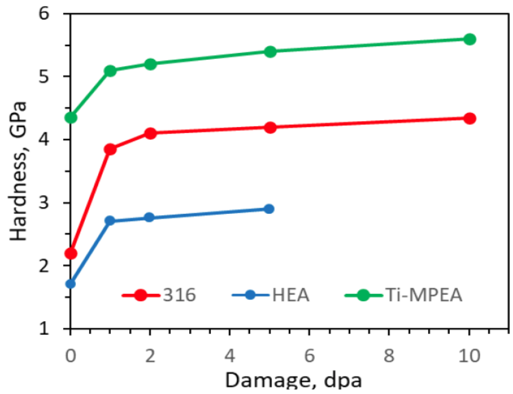

Fig. 15. The dose dependences of bulk-equivalent hardness for 20Cr40Fe20Mn20Ni (HEA), 61Ti10Cr7Al11V11Nb (Ti-MPEA), and SS316 for comparison

The irradiation temperature significantly affects the formation and evolution of defect microstructures. Defect clusters are observed to grow when the irradiation temperature is high enough to promote the diffusion of irradiation-induced defects. However, if the irradiation temperature exceeds a certain threshold, point defects are emitted from the clusters, promoting their recombination and thereby reducing the density of defect clusters [69, 70].

For instance, a study examining the influence of irradiation temperature on the mechanical properties of Fe-implanted Fe-Cr alloys up to 0.6 dpa demonstrated that there was no observable hardening when implantation occurred at 500 °C [71]. In another study, the irradiation hardening of Fe-ion irradiated Fe-2.5 at.%Cr, Fe-9 at.%Cr, and Fe-12.5 at.%Cr was characterized at room temperature, 300 and 500 °C. It was found that no radiation hardening occurred for

Fe-2.5 at.%Cr and Fe-9 at.%Cr at 500 °C. However, a notable enhancement in irradiation hardening was discerned for Fe-12.5 at.%Cr at each temperature, which can be attributed to the generation of α' particles under Fe irradiation [72].

The temperature dependence of irradiation hardening in various Fe-Cr alloys is shown in Fig. 16 [73]. It can be clearly seen that irradiation hardening strongly depends on the irradiation temperature, and almost no hardening was observed at temperatures above 500 °C, that correlates with the temperature dependence of loop density (see Fig. 9).

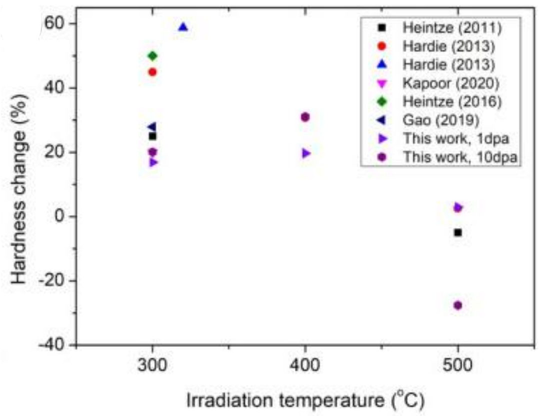

Fig. 16. Irradiation hardening of various Fe-Cr alloys (8…9% Cr) irradiated with Fe ions at 300…500 °C, as previously reported in [73]. The underlying data are derived from [8, 71, 72, 74–76]

In the case of noble gas irradiation, the role of irradiation temperature appears to be more complex. Specifically, irradiation temperature plays a crucial role in determining the irradiation hardening behavior of materials implanted with helium or argon ions [62, 77, 78].

4. IRRADIATION HARDENING OF SELECTED STRUCTURAL ALLOYS

This section addresses the hardening/embrittlement phenomenon under ion irradiation in relation to a series of recently synthesized/modified alloys, encompassing multi-principal element alloys with FCC and BCC phase structures, as well as ODS-modified austenitic steel and ferritic-martensitic steel subjected to severe plastic deformation (SPD). The nanohardness profiles as a function of indenter displacement are measured for both unirradiated and irradiated (with 1.4 MeV Ar^+ ions) samples, and the bulk-equivalent hardness (H_0) is calculated by applying the Kasada approach [21]. A comparative analysis is performed with data for conventional stainless steels under identical irradiation conditions.

4.1. ODS-MODIFIED AUSTENITIC STEELS

The microstructure of as-received 18Cr10NiTi-ODS steel is characterized by fine grains with an average size of ~1.2 μm (Fig. 17,a) [62]. Within the matrix of each grain, high-density oxide nanoprecipitates were observed with a nearly uniform distribution (see Fig. 17,b). The size of these precipitates ranges from several nanometers to hundreds of nanometers; however, the larger precipitates are significantly lower in density, resulting in their contribution to both concentration and average size being negligible. The average size of the nanoprecipitates is estimated to be ~10 nm, with an average density of $\sim 7.3 \cdot 10^{21}$ m^{-3}. Electron microprobe analysis revealed the presence of Y, Zr, Ti, and O within these precipitates. Further investigation using electron diffraction identified these precipitates as complex oxides with a pyrochlore structure, specifically $Y_2(Zr,Ti)_2O_7$ [62].

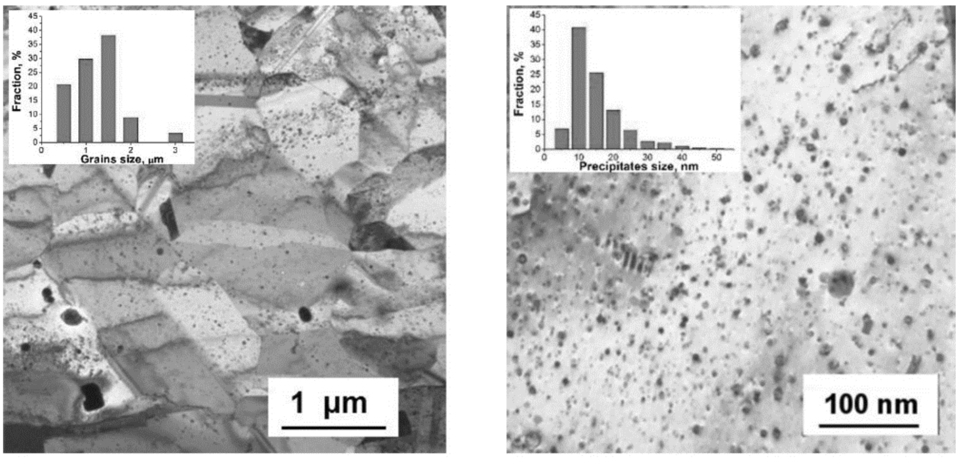

a *b*

Fig. 17. Preirradiation microstructure of 18Cr10NiTi-ODS steel: a – grain structure, also showing nanooxides, and grain size distribution; b – nanooxide precipitates in the matrix at higher magnification and size distribution of nanoprecipitates [62]

It appears that the differences in hardness between ODS-modified (3.2 GPa) and conventional steel (2.2 GPa) may be attributed to the microstructural features revealed by TEM. A microstructure composed of finer grains generally results in increased strength and improved toughness compared to an identical alloy with coarser grains. Additionally, the presence of dispersed ultrafine particles plays a crucial role in impeding dislocation motion, thereby contributing to precipitation strengthening. As a result, the observed increase in hardness in the as-received 18Cr10NiTi-ODS steel can be attributed to the synergistic effects of grain refinement and the distribution of oxide nanoprecipitates [62].

The degree of radiation-induced hardening was also observed to vary significantly at low and elevated irradiation temperatures (Fig. 18), which can be attributed to variations in microstructure.

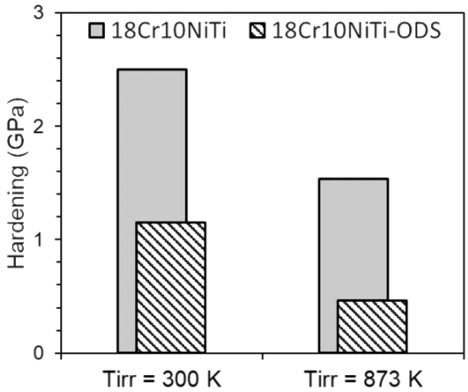

Fig. 18. The hardening of 18Cr10NiTi and 18Cr10NiTi-ODS steels irradiated to 50 dpa at T_{room} and 873 K

As illustrated in Fig. 18, the degree of irradiation-induced hardening observed in 18Cr10NiTi-ODS is found to be less pronounced than that observed in conventional steel. This reduction in hardening can be attributed to the high density of grain boundaries and the presence of dispersed ultrafine oxide particles within the 18Cr10NiTi-ODS matrix, which act as effective sinks for point defects generated during irradiation. The incorporation of a substantial density of point defect recombination centers and point defect sinks has been identified as an effective strategy for the development of radiation-tolerant materials. This approach is supported by kinetic rate theory models [79, 80], which indicate that the presence of high sink strengths leads to a marked decrease in point defect supersaturation, thereby mitigating phenomena such as void swelling and radiation-induced solute segregation [81]. Furthermore, ODS modifications that enhance sink strength contribute to the effective mitigation of low-temperature radiation-induced hardening. Consequently, the 18Cr10NiTi-ODS may demonstrate a reduced susceptibility to radiation-induced embrittlement, thereby enhancing its applicability in advanced nuclear environments.

4.2. FCC AND BCC MULTI-PRINCIPAL ELEMENT ALLOYS

A non-cobalt high-entropy alloy (hereinafter referred to as HEA) with a composition of 20Cr40Fe20Mn20Ni (mass %) was produced via arc melting in a water-cooled copper mold under a high-purity argon atmosphere. X-ray diffraction (XRD) analysis indicated that the as-cast alloy, subsequent to a final heat treatment at 1100 °C, exhibited a single-phase FCC crystal lattice. The average grain size of the HEA was measured to be 3.47 μm (Fig. 19). The initial dislocation densities were found to range from 1.7 to $2.5 \cdot 10^{12}$ m^{-2} [82].

The new lightweight multi-principal element titanium-based alloy 61Ti10Cr7Al11V11Nb (at.%) with non-equal molar ratio, referred to as Ti-MPEA, was obtained by arc melting using a non-consumable tungsten electrode in a pure argon atmosphere [68, 83].

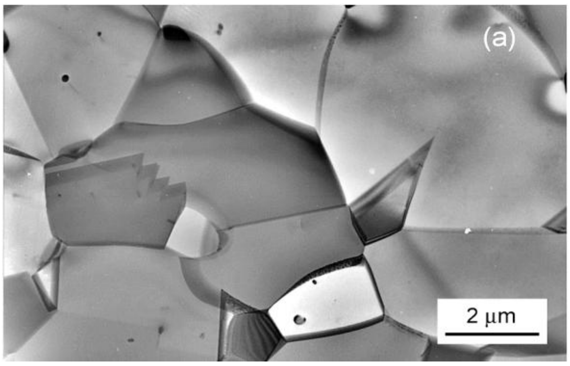

Fig. 19. Typical TEM micrograph of 20Cr40Fe20Mn20Ni high-entropy alloy [82]

The initial microstructure of the Ti-MPEA alloy prior to irradiation is presented in Fig. 20. XRD analysis indicates that the alloy possesses a single BCC structure, with no evidence of secondary phases. Notably, the Ti-MPEA alloy exhibited a high intrinsic hardness of 4.3 GPa even before irradiation, despite its coarse grain size and the apparent absence of nanoprecipitates (as shown in Fig. 20). This significant hardness is likely attributable to solid-solution hardening, which occurs when the addition of various soluble elements enhances the strength of the matrix. The resulting lattice distortion due to atomic radius mismatch impedes dislocation movement, thereby increasing hardness [84].

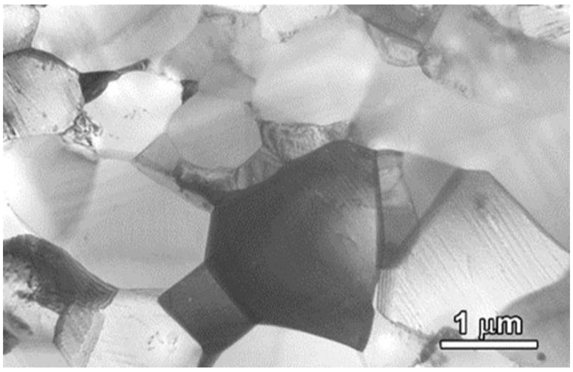

Fig. 20. TEM micrograph of 61Ti10Cr7Al11V11Nb alloy after annealing at 900 °C for 15 min

The radiation-induced hardening of HEA, Ti-MPEA, and SS316 as a reference material is presented in Fig. 21. The data was obtained after irradiation of materials with 1.4 MeV Ar^{+} ions under identical conditions.

Although the BCC-phase Ti-MPEA exhibits exceptionally high intrinsic hardness even prior to irradiation [80], the magnitude of radiation hardening for ion-irradiated Ti-based MPEA was significantly smaller compared to that observed for FCC-HEA and SS316.

In general case, the observed increase in hardness can be explained by widely accepted models [85, 86] that suggest the presence of irradiation defect clusters, such as dislocation loops, which impede the glide of dislocations. However, HEAs possess specific characteristics, such as high mixing entropy in thermodynamic properties and lattice distortion effects in their structure, which appear to contribute to a lower defect density compared to conventional steels.

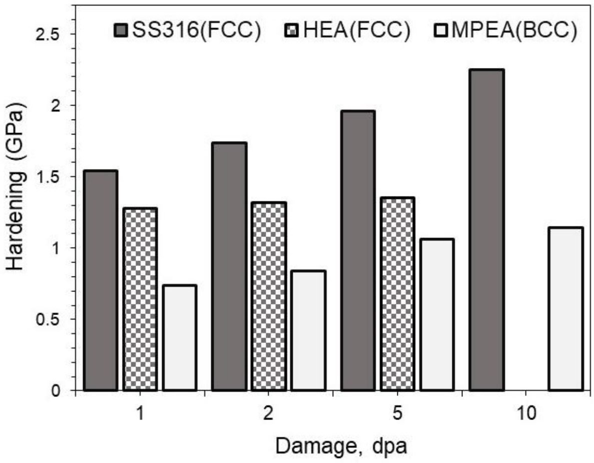

Fig. 21. The radiation hardening versus damage

Moreover, the primary mechanism underlying recovery in multicomponent concentrated alloys has been identified as the recombination of vacancies and interstitials. This phenomenon can be attributed to the increased compositional complexity and the variations in atomic sizes among the principal elements that constitute the alloy [87]. Additionally, atomistic simulations and experimental studies have indicated that the suppression of accumulated damage levels in more complex and disordered alloys may be linked to modified migration barriers and limited atomic diffusion [88]. The energy barrier associated with an atom's movement between positions with differing lattice potential energies makes this process energetically unfavorable, resulting in a decreased overall mobility of interstitials and vacancies. This prevents the formation and growth of vacancy clusters and dislocation loops while facilitating the recombination of vacancy-interstitial pairs.

A detailed examination of irradiation hardening behavior across a broad spectrum of HEA materials was recently presented in [89]. It is noteworthy that previous investigations of the effects of irradiation on HEAs have primarily focused on irradiation damage levels of up to 20 dpa. This value is significantly lower than the target specifications for future advanced nuclear energy systems, which aim for approximately 200 dpa. However, it is important to highlight that a marked increase in hardness is observed within a few dpa across a wide array of materials studied. As the irradiation dose continues to increase, the hardening process gradually approaches saturation (Fig. 22).

The analysis of Fig. 22 demonstrates that the irradiation-induced hardening observed in certain BCC-phase HEAs is markedly lower in comparison to both FCC-phase HEAs and conventional alloys. This observation indicates that BCC-phase HEAs have a higher resistance to irradiation hardening than conventional alloys. This advantage can be attributed to the higher stacking fault energies and greater lattice distortion in BCC-phase HEAs relative to their FCC-phase HEA counterparts.

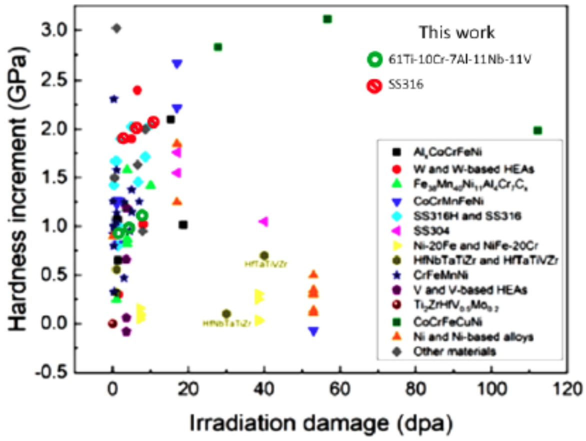

Fig. 22. Irradiation hardness increment, ΔH, versus irradiation damage. The data for comparison is taken from [89, 68]

4.3. SPD-MODIFIED FERRITIC-MARTENSITIC STEEL

High chromium ferritic-martensitic steels are well known to experience significant degradation in mechanical properties due to radiation effects, particularly through irradiation hardening and embrittlement at low temperatures (≤ 160 °C). Notably, substantial hardening can occur at irradiation doses as low as 0.01 dpa. Therefore, it is crucial to implement strategies to mitigate radiation hardening and embrittlement in these materials.

It is established that the factors capable of enhancing the properties of materials include grain size reduction, optimization of composition, and the control of quantity, size, and distribution of secondary phases [90]. Severe plastic deformation represents one of the most effective methods of grain size control in alloys. It allows the creation of a submicrocrystalline or nanocrystalline state in steels, which has a positive effect on increasing the strength and radiation resistance of steel [91]. The combination of this method with heat treatment allows for the optimization of secondary phase separation parameters. The method of multi-cycle or multiple "deposition-extrusion", developed at NSC KIPT [92], was applied as SPD. This method has been shown to be effective in producing ultrafine grained materials in both laboratory and industrial contexts.

T91 ferritic-martensitic steel, with a composition of 9Cr-1Mo and minor alloying elements of Ni, Nb, V, and C, was supplied as hot-rolled and heat-treated plates with a thickness of 40 mm. The heat treatment process included normalization at 1040 °C for 30 min, followed by air cooling, and subsequent tempering at 730 °C for 60 min followed by air cooling to room temperature. The microstructure of the as-received T91 steel (referred to as T91-M) is characterized by a tempered martensite structure with the occurrence of boundaries of former austenite grains and subgrains (Fig. 23). These boundaries are decorated with precipitates of $M_{23}C_6$ carbides. The average size of the former austenite grains is ~ 20 µm, and the average size of subgrains is ≈ 8 µm. Within the former austenite grains, martensite lamellae with transverse dimensions of 0.25 to 0.5 µm are observed. Additionally, a significant number of small precipitates, typically referred to as MX-type phases, with sizes of ≤ 50 nm are also present [93].

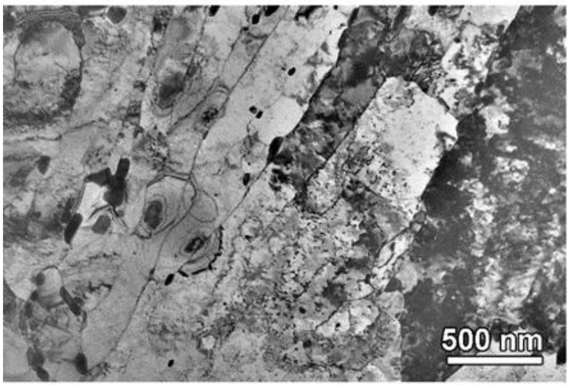

Fig. 23. Microstructure of as-received T91-M steel

An applying of SPD using the “upsetting-extrusion” method resulted in a significant reduction in the average grain size, decreasing from 8 μm in the as-received state to 100 nm following SPD of T91 steel (referred to as T91-MSPD) (Fig. 24). Subsequent heat treatment at 600 °C for 25 h led to the formation of sufficiently large grains with a typical “ferritic” morphology. In some regions, the "broken" martensite structure was transformed into a more classical form [93].

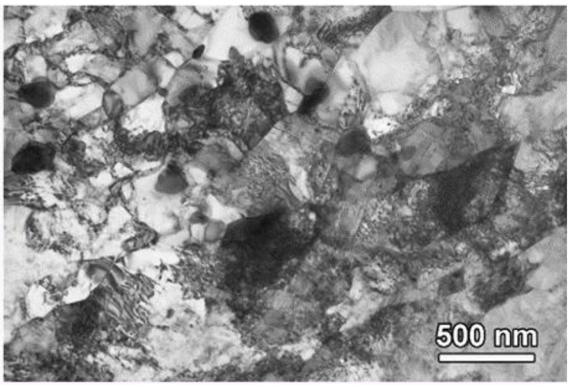

Fig. 24. Microstructure of T91-MSPD

As a consequence of this treatment, the hardness of unirradiated T91-MSPD was enhanced; however, the radiation hardening exhibited no noticeable difference between the two steel modifications (Fig. 25). For unirradiated T91-MSPD samples, the hardness H_0 was measured at 3.9 GPa, while for the as-received T91-M samples, this value was 2.98 GPa. The significant increase in hardness observed in T91-MSPD is attributed to grain refinement, fragmentation of lamellas, a reduction in MX carbide size, and their more uniform distribution.

Irradiation of T91-MSPD and T91-M with 1.4 MeV argon ions revealed that radiation hardening tends to reach saturation at around a few dpa. Furthermore, the irradiation hardening degree of T91-MSPD and T91-M is nearly equivalent when the irradiation dose is approximately 10 dpa. Despite differences in initial strength and sink density between T91-M and T91-MSPD steels, the formation of defect clusters and Ar-associated nano-bubbles appears to similarly influence the hardening behavior of both steels under argon-ion irradiation at doses higher than 10 dpa (see Fig. 25).

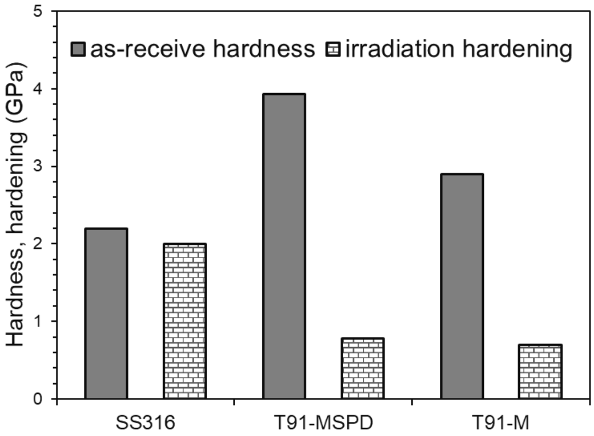

Fig. 25. As-received hardness and relative irradiation-induced hardening of steels T91-M, T91-MSPD, and SS316 for comparison (10 dpa, T_{room})

A comparison of radiation-induced hardening in ferritic-martensitic steels, as reported by various authors [25, 26, 29, 76, 94–98] (Fig. 26), reveals some discrepancies in the data, likely attributable primarily to differences in irradiation temperatures. Furthermore, significant variations are observed depending on the material's microstructure. For example, alloys with ferritic structures exhibit a hardness increase (ΔH) of 0.95 GPa, whereas tempered martensitic alloys show a ΔH of 0.58 GPa at low doses of 2…3 dpa. At a dose of 30 dpa, these values are reported as 1.32 and 0.85 GPa, respectively [93, 94]. This suggests that the fine microstructure of tempered martensite significantly reduces the degree of hardening under irradiation. The ultra-fine-grained structure of ferritic-martensitic T91-MSPD steel, characterized by a high density of grain boundaries, acts as an effective absorber of radiation defects. Consequently, the formation of obstacles to dislocation movement is expected to be less pronounced in F-M steels with a high density of initial traps or sinks for radiation defects. As a result, ferritic-martensitic steels are less susceptible to radiation hardening and embrittlement compared to materials with purely ferritic microstructures.

The degree of hardening of T91-M and T91-MSPD steels (see Fig. 25) as well as Ti-MPEA (see Fig. 21), which are all BCC-structured alloys, is approximately half that of the austenitic reference steels, suggesting a reduced propensity for embrittlement. BCC metals are typically regarded as exhibiting superior radiation tolerance in comparison to FCC metals. This assumption is primarily supported by extensive research indicating that F-M steels, which possess a BCC structure, exhibit significantly less void swelling than their austenitic (FCC) counterparts under identical irradiation conditions.

The research findings indicate that BCC metals exhibit superior performance in comparison to FCC metals with respect to primary defect production and defect evolution behavior [99, 100]. BCC metals demonstrate not only a lower overall fraction of large defect clusters but also a more finely dispersed distribution of these clusters within energetic displacement cascades.

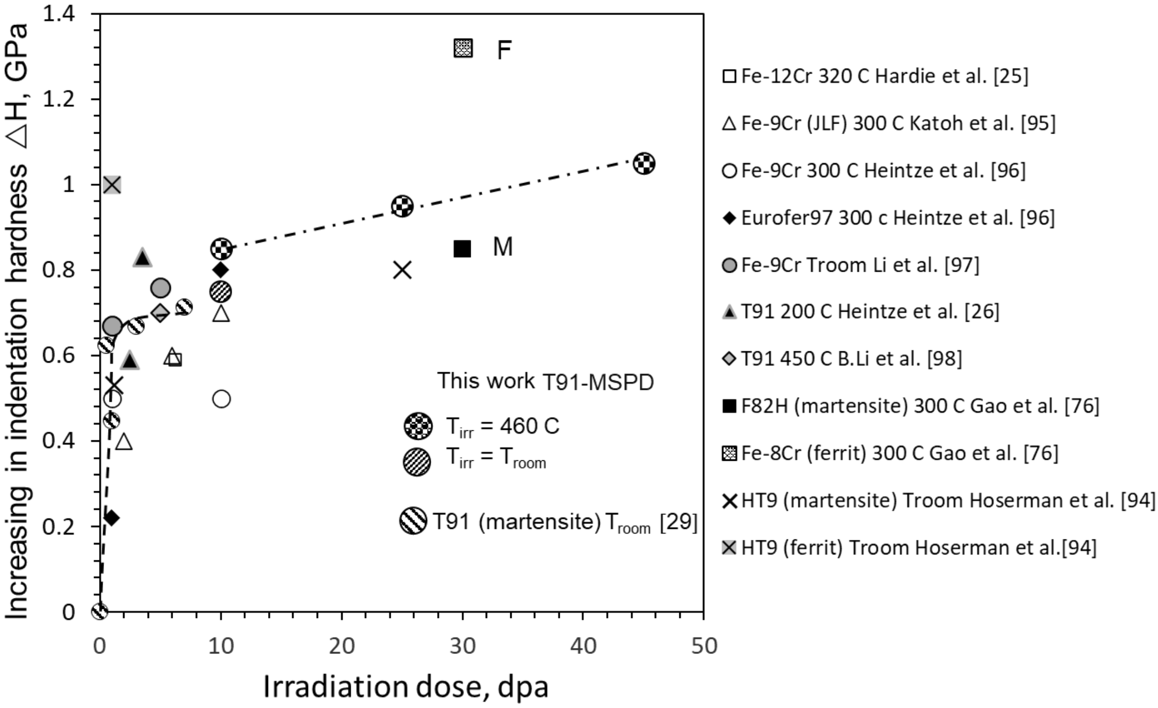

Fig. 26. Relative radiation-induced hardening of ferritic-martensitic steels. Dotted and dash-dotted lines are drawn for eyes only

The fine dispersion of primary defects can facilitate more efficient defect recombination during subsequent microstructural evolution, thereby enhancing the radiation resistance of BCC metals.

Although BCC materials have been observed to exhibit superior radiation resistance, the underlying physical mechanisms remain poorly understood. Potential contributing factors have been suggested to include reduced in-cascade production of sessile point defect clusters, lower dislocation bias, and higher self-diffusion coefficients. The latter is known to be generally higher in BCC metals at a given homologous temperature, which enhances self-recovery diffusion mechanisms and suppresses radiation damage accumulation [101].

SUMMARY

This review analyzed the phenomenon of irradiation-induced hardening in relation to a range of nuclear structural materials, with a focus on ODS-modified austenitic steels, ferritic-martensitic steels, and high-entropy alloys due to their unique properties and responses to irradiation, which are critical for advanced nuclear applications. Ion irradiation combined with nanoindentation has been utilized to study these materials, examining both experimental findings and theoretical approaches to elucidate the mechanisms underlying radiation-induced hardening.

The study investigated the nanohardness of materials in their initial state, analyzed the dependence of hardening parameters on irradiation dose, and explored the correlation between these parameters and microstructural evolution. It was found that dislocation loops and gas-filled nanosized bubbles are the primary contributors to irradiation hardening.

The advanced alloys studied demonstrated lower susceptibility to irradiation-induced hardening compared to conventional austenitic stainless steels. This was attributed to various mechanisms, including enhanced sink strength for radiation defects in ODS-modified steels, which mitigates low-temperature hardening. HEA materials showed reduced hardening due to high configurational entropy and sluggish diffusion. BCC-structured alloys exhibited approximately 50% less hardening than austenitic reference steels, suggesting more efficient defect recombination and higher self-diffusion coefficients, contributing to their lower susceptibility to embrittlement.

ACKNOWLEDGEMENTS

The work was financially supported by the National Academy of Science of Ukraine (program “Fundamental scientific research on the most important problems of the development of scientific and technical, socio-economic, socio-political, human potential to ensure Ukraine's competitiveness in the world and sustainable development of society and the state”).

REFERENCES

1. S.J. Zinkle, G. Was. Materials challenges in nuclear energy // *Acta Mater*. 2013, v. 61 (3), p. 735-758.

2. S.J. Zinkle, J.T. Busby. Structural materials for fission and fusion energy // *Mater. Today*. 2009, v. 12 (11), p. 12-19.

3. V.N. Voyevodin and I.M. Neklyudov. *Evolution of the Structural-Phase State and Radiation Resistance of Structural Materials.* Kiev: “Naukova Dumka”, 2006.

4. P. Hosemann. Small-scale mechanical testing on nuclear materials: bridging the experimental length-scale gap // *Scr. Mater*. 2018, v. 143, p. 161-168.

5. M. Saleh, Z. Zaidi, C. Hurt, M. Inoescu, P. Munroe, D. Bhattacharyya. Comparative study of two

nanoindentation approaches for assessing mechanical properties of ion-irradiated stainless steel 316 // *Metals*. 2018, v. 8, p. 719-724.

6. P. Hosemann, C. Shin, D. Kiener. Small scale mechanical testing of irradiated materials // *J. Mater. Res*. 2015, v. 30, p. 1231-1245.

7. G.N. Tolmachova, G.D. Tolstolutskaya, and S.A. Karpov. Application of nanoindentation for investigation of radiation damage in SS316 stainless steel // *PAST*. 2015, N 5, p. 168-173.

8. C.D. Hardie, S.G. Roberts. Nanoindentation of model Fe–Cr alloys with self-ion irradiation // *J. Nucl. Mater*. 2013, v. 433, p. 174-179.

9. C. Heintze, I. Hilger, F. Bergner, T. Weissgaerber, B. Kieback. Nanoindentation of single- (Fe) and dual-beam (Fe and He) ion-irradiated ODS Fe–14Cr-based alloys: effect of the initial microstructure on irradiation-induced hardening // *J. Nucl. Mater*. 2019, v. 518, p. 1-10.

10. A. Kareer, A. Prasitthipayong, D. Krumwiede, D.M. Collins, P. Hosemann, S.G. Roberts. An analytical method to extract irradiation from nanoindentation hardness-depth curves // *J. Nucl. Mater*. 2018, v. 498, p. 274-281.

11. S.A. Karpov, G.D. Tolstolutskaya, V.N. Voyevodin, G.N. Tolmachova, I.E. Kopanets. The dose dependence of inert gases irradiation hardening of 316 austenitic stainless steel after low temperature irradiation // *PAST*. 2018, N 5(117), p. 34-39.

12. G.M. Pharr, W.C. Oliver. Nanoindentation of silver-relations between hardness and dislocation structure // *J. Mater. Res*. 1989, v. 4.1, p. 94-101.

13. W.D. Nix. Mechanical properties of thin films // *Metallurgical Mater. Trans. A*. 1989, v. 20 (11), p. 2217-2245.

14. A.A. Elmustafa, D.S. Stone. Indentation size effect in polycrystalline FCC metals // *Acta Mater*. 2002, v. 50 (14), p. 3641-3650.

15. G.Z. Voyiadjis, R. Peters. Size effects in nanoindentation: an experimental and analytical study // *Acta Mech*. 2010, v. 211.1, p. 131-153.

16. W.D. Nix, H.J. Gao. Indentation size effects in crystalline materials: A law for strain gradient plasticity // *J. Mech. Phys. Solid*. 1998, v. 46, p. 411-425.

17. H. Gao, Y. Huang, W.D. Nix, J.W. Hutchinson. Mechanism-based strain gradient plasticity-I. Theory // *J. Mech. Phys. Solids*. 1999, v. 47 (6), p. 1239-1263.

18. Y. Huang, H. Gao, W.D. Nix, J.W. Hutchinson. Mechanism-based strain gradient plasticity-II Analysis // *J. Mech. Phys. Solids*. 2000, v. 48 (1), p. 99-128.

19. G.M. Pharr, E.G. Herbert, Y. Gao. The indentation size effect: a critical examination of experimental observations and mechanistic interpretations // *Annu. Rev. Mater. Res*. 2010, v. 40, p. 271-292.

20. T.S. Byun, K. Farrell. Irradiation hardening behavior of polycrystalline metals after low temperature irradiation // *J. Nucl. Mater*. 2004, v. 326, p. 86-96.

21. R. Kasada et al. A new approach to evaluate irradiation hardening of ion-irradiated ferritic alloys by nano-indentation techniques // *Fusion Eng. Des.* 2011, v. 86, p. 2658-2661.

22. P. Hosemann, D. Kiener, Y. Wang, S. Maloy. Issues to consider using nanoindentation on shallow ion beam irradiated materials // *J. Nucl. Mater*. 2012, v. 425 (1-3), p. 136-139.

23. Y.Y. Lim, M.M. Chaudri. The effect of the indenter load on the nanohardness of ductile metals: an experimental study on polycrystalline work- hardened and annealed oxygen-free copper // *Phil. Mag. A.* 1999, v. 79, p. 2979-3000.

24. Y. Wang, D. Raabe, C. Klueber, F. Roters. Orientation dependence of nanoindentation pile-up patterns and of nanoindentation microtextures in copper single crystals // *Acta Mater*. 2004, v. 52, p. 2229-2238.

25. C.D. Hardie, S.G. Roberts, and A.J. Bushby. Understanding the effects of ion irradiation using nanoindentation techniques // *J. Nucl. Mater*. 2015, v. 462, p. 391-401.

26. C. Heintze, F. Bergner, S. Akhmadaliev, E. Altstadt. Ion irradiation combined with nanoindentation as a screening test procedure for irradiation hardening // *J. Nucl. Mater*. 2016, v. 472, p. 196-205.

27. C.E. Beck, F. Hofmann, J.K. Eliason, A.A. Maznev, K.A. Nelson, and D.E.J. Armstrong. Correcting for contact area changes in nanoindentation using surface acoustic waves // *Scr. Mater*. 2017, v. 128, p. 83-86.

28. T.Y. Tsui, G.M. Pharr. Substrate effects on nanoindentation mechanical property measurement of soft films on hard substrates // *J. Mater. Res*. 1998, v. 14, p. 292-301.

29. V.N. Voyevodin, G.D. Tolstolutskaya, S.A. Karpov, M.A. Tikhonovsky, G.N. Tolmachova, A.S. Kalchenko, R.L. Vasilenko, I.E. Kopanets. Effect of argon ion irradiation on hardening and microstructure of ferritic-martensitic steel T91 // *PAST*. 2019, N 2(120), p. 7-12.

30. T.S. Byun, K. Farrell, M. Li. Deformation in metals after low-temperature irradiation: Part I – Mapping macroscopic deformation modes on true stress-dose plane // *Acta Mater*. 2008, v. 56, p. 1044-1055.

31. T.S. Byun, K. Farrell, M. Li. Deformation in metals after low-temperature irradiation: Part II – Irradiation hardening, strain hardening, and stress ratios // *Acta Mater*. 2008, v. 56, p. 1056-1064.

32. E. Getto, M. Johnson, M. Maughan, et al. Friction stir welding and self-ion irradiation effects on microstructure and mechanical properties changes within oxide dispersion strengthened steel MA956 // *J. Nucl. Mater*. 2002, v. 567, p. 153795.

33. S.A. Karpov, I.E. Kopanets, V.V. Ruzhytskyi, B.S. Sungurov, G.D. Tolstolutskaya. Cooperative effect of displacement damage and inert gas impurities on deuterium retention in austenitic and ferritic-martensitic steels // *PAST*. 2014, N 4(9), p. 31-37.

34. S. Zinkle, P. Maziasz, R. Stoller. Dose dependence of the microstructural evolution in neutron-irradiated austenitic stainless steel // *J. Nucl. Mater*. 1993, v. 206 (2-3), p. 266-286.

35. S. Hamada, M. Suzuki, P.J. Maziasz, A. Hishinuma, M.P. Tanaka. The microstructural evolution and swelling behavior of type 316 stainless steel

irradiated in HFIR, in: Effects of Radiation on Materials: 14th International Symposium (v. I), ASTM International, 1990.

36. H. Brager, F. Garner, E. Gilbert, J. Flinn, W. Wolfer. Stress-affected microstructural development and creep-swelling interrelationship, in: Conference on radiation effects in breeder reactor structural materials, 1977.

37. X. Liu, J. Stubbins. Fundamental Studies of Irradiation-Induced Modifications in Microstructural Evolution and Mechanical Properties of Advanced Alloys // *Final Report*. 2018, April 24.

38. P. Maziasz. Temperature dependence of the dislocation microstructure of PCA austenitic stainless steel irradiated in ORR spectrally-tailored experiments // *J. Nucl. Mater*. 1992, v. 191-194, p. 701-705.

39. H. Brager, J. Straalsund. Defect development in neutron irradiated type 316 stainless steel // *J. Nucl. Mater*. 1973, v. 46 (2), p. 134-158.

40. H. Brager, L. Blackburn, D. Greenslade. The dependence on displacement rate of radiation-induced changes in microstructure and tensile properties of AISI 304 and 316 // *J. Nucl. Mater*. 1984, v. 122 (1-3), p. 332-337.

41. H. Kawanishi, S. Ishino. Microstructure of Fe–16Ni–15Cr alloys irradiated in JOYO // *J. Nucl. Mater*. 1988, v. 155-157, p. 806-809.

42. H. Kawanishi, S. Ishino. Characterization of microstructure at 673 K in neutron-irradiated Fe–16Ni–15Cr with the addition of C, Ti and Nb // *J. Nucl. Mater*. 1991, v. 179-181, p. 534-537.

43. T. Sawai, P. Maziasz, A. Hishinuma. Microstructural evolution of welded austenitic stainless steels irradiated in the spectrally-tailored ORR experiment at 400 °C // *J. Nucl. Mater*. 1991, v. 179-181, p. 519-522.

44. N. Yoshida, Q. Xu, H. Watanabe, T. Muroga, M. Kiritani. Low dose fission neutron irradiation on P- and Ti-modified austenitic alloys with improved temperature control // *J. Nucl. Mater*. 1992, v. 191-194, p. 1114-1118.

45. E. Bloom, J. Stiegler. Effect of irradiation on the microstructure and creep-rupture properties of type 316 stainless steel // *Effects of Radiation on Substructure and Mechanical Properties of Metals and Alloys, ASTM International,* 1973.

46. H. Brager. The effects of cold working and pre-irradiation heat treatment on void formation in neutron-irradiated type 316 stainless steel // *J. Nucl. Mater*. 1975, v. 57 (1), p. 103-118.

47. H. Brager, F. Garner, G. Guthrie. The effect of stress on the microstructure of neutron irradiated type 316 stainless steel // *Journal of Nuclear Materials.* 1977, v. 66 (3), p. 301-321.

48. P. Barton, B. Eyre, D. Stow. The structure of fast-reactor irradiated solution-treated AISI type 316 steel // *J. Nucl. Mater*. 1977, v. 67 (1-2), p. 181-197.

49. P. Maziasz. Microstructures developed in austenitic stainless steels irradiated in HFIR at 552 °C // *Trans. Am. Nucl. Soc. (United States).* 1981, v. 39.

50. M. Tanaka, S. Hamada, A. Hishinuma, P. Maziasz. Microstructural development of austenitic stainless steels irradiated in HFIR // *J. Nucl. Mater*. 1988, v. 155-157, p. 801-805.

51. P. Maziasz. Overview of microstructural evolution in neutron-irradiated austenitic stainless steels // *J. Nucl. Mater*. 1993, v. 205, p. 118-145.

52. P. Maziasz. Formation and stability of radiation-induced phases in neutron-irradiated austenitic and ferritic steels // *J. Nucl. Mater*. 1989, v. 169, p. 95-115.

53. D. Edwards, E. Simonen, F. Garner, L. Greenwood, B. Oliver, S. Bruemmer. Influence of irradiation temperature and dose gradients on the microstructural evolution in neutron-irradiated 316SS // *J. Nucl. Mater*. 2003, v. 317 (1), p. 32-45.

54. R. Klueh, A. Nelson. Ferritic/martensitic steels for next-generation reactors // *J. Nucl. Mater*. 2007, v. 371 (1-3), p. 37-52.

55. R.L. Klueh. Elevated temperature ferritic and martensitic steels and their application to future nuclear reactors // *International Materials Reviews*. 2005, v. 50 (5), p. 287-310.

56. S. L. Dudarev, R. Bullough, P. M. Derlet. Effect of the α-γ-phase transition on the stability of dislocation loops in bcc iron *// Physical Review Letters.* 2008, v. 100 (13), p. 135503.

57. M. Ando, E. Wakai, T. Sawai, H. Tanigawa, K. Furuya, S. Jitsukawa, H. Takeuchi, K. Oka, S. Ohnuki, A. Kohyama. Synergistic effect of displacement damage and helium atoms on radiation hardening in f82h at tiara facility // *J. Nucl. Mater*. 2004, v. 333-329, p. 1137-1141.

58. Y.N. Osetsky, D.J. Bacon. Atomic-scale mechanisms of void hardening in bcc and fcc metals // *Phil. Mag*. 2010, v. 90 (7-8), p. 945-961.

59. R.E. Stoller, G.R. Odette. The effects of helium implantation on microstructural evolution in an austenitic alloy // *J. Nucl. Mater*. 1988, v. 154, p. 286-304.

60. H. Zhang, C. Zhang, Y. Yang, Y. Meng, J. Jang, A. Kimura. Irradiation hardening of ODS ferritic steels under helium implantation and heavy-ion irradiation // *J. Nucl. Mater*. 2014, v. 455, p. 349-353.

61. P. Dayal, D. Bhattacharyya, W.M. Mook, E.G. Fu, Y.Q. Wang, D.G. Carr, O. Anderoglu, N.A. Mara, A. Misra, R.P. Harrison, L. Edwards. Effect of double ion implantation and irradiation by Ar and He ions on nano-indentation hardness of metallic alloys // *J. Nucl. Mater*. 2013, v. 438, p. 108-115.

62. A.N. Velikodnyi, V.N. Voyevodin, A.S. Kalchenko, S.A. Karpov, I.V. Kolodiy, M.A. Tikhonovsky, G.D. Tolstolutskaya, F.A. Garner. Impact of nano-oxides and injected gas on swelling and hardening of 18Cr10NiTi stainless steel during ion irradiation // *J. Nucl. Mater*. 2022, v. 565, p. 153666.

63. S.M. Hafez Haghighat, R. Schaublin. Influence of the stress field due to pressurized nanometric He bubbles on the mobility of an edge dislocation in iron // *Phil. Mag*. 2010, v. 90, p. 1075-1100.

64. V.I. Dubinko, S.A. Kotrechko, V.F. Klepikov. Irradiation hardening of reactor pressure vessel steels due to the dislocation loop evolution // *Radiat. Eff. Def. Solids*. 2009, v. 164 (10), p. 647-655.

65. S.A. Karpov, G.D. Tolstolutskaya, B.S. Sungurov, A.Yu. Rostova, G.N. Tolmacheva, I.E. Kopanets.

Hardening of SS316 stainless steel caused by the irradiation with argon ions // *Materials Science.* 2016, v. 52, N 3, p. 377-384.

66. B.N. Singh, A.J.E. Foreman, H. Trinkaus. Radiation hardening revisited: role of intracascade clustering // *J. Nucl. Mater*. 1997, v. 249, p. 103-115.

67. A.F. Rowcliffe, S.J. Zinkle, J.F. Stubbins, D.J. Edwards, D.J. Alexander. Austenitic stainless steels and high strength copper alloys for fusion components // *J. Nucl. Mater.* 1998, v. 258-263, p. 183-191.

68. G. Tolstolutska, M. Tikhonovsky, O. Velikodnyi, S. Karpov, V. Ruzhytskyi, G. Tolmachova, R. Vasilenko. Hardening of lightweight multi-principal element titanium-based alloy under Ar ion irradiation // *PAST*. 2023, N 5(147), p. 3-8.

69. M. Kolluri, P.D. Edmondson, N.V. Luzginova, F.A. Vander Berg. Influence of irradiation temperature on microstructure of EU batch of ODS Eurofer97 steel irradiated with neutrons // *Mater. Sci. Technol*. 2014, v. 30, p. 1697-1703.

70. M. Klimenkov, A. Moeslang, E. Materna-Morris. Helium influence on the microstructure and swelling of 9%Cr ferritic steel after neutron irradiation to 16.3 dpa // *J. Nucl. Mater*. 2014, v. 453, p. 54-59.

71. C.D. Hardie, C.A. Williams, S. Xu, S.G. Roberts. Effects of irradiation temperature and dose rate on the mechanical properties of self-ion implanted Fe and Fe-Cr alloys // *J. Nucl. Mater*. 2013, v. 439, p. 33-40.

72. C. Heintze, F. Bergner, M.H. Mayoral. Ion-irradiation-induced damage in Fe-Cr alloys characterized by nanoindentation // *J. Nucl. Mater*. 2011, v. 417, p. 980-983.

73. Haiying Fu, Bingsheng Li, Shuai Xu, Hongfeng Zhu, Shilei Han, Rongrong Luo, Hongbin Liao, Xiaoyu Wang, Jiming Chen, Pengyuan Li. Effect of irradiation temperature on radiation hardening of CLF-1 steel // *Fusion Engineering and Design*. 2023, v. 189, p. 113488.

74. G. Kappor, P. Chekhonin, C. Kaden, K. Vogel, F. Bergner. Microstructure-informed prediction and measurement of nanoindentation hardness of an Fe-9Cr alloy irradiated with Fe-ions of 1 and 5 MeV energy // *Nucl. Mater. and Eng*. 2022, v. 30, p. 101105.

75. C. Heintze, F. Bergner, M.H. Mayoral, R. Kogler, G. Muller, A. Ulbricht. Irradiation hardening of Fe-9Cr-based alloys and ODS Eurofer: effect of helium implantation and iron-ion irradiation at 300 °C including sequence effects // *J. Nucl. Mater*. 2016, v. 470, p. 258-267.

76. J. Gao, K. Yabuuchi, A. Kimura. Ion-irradiation hardening and microstructure evolution in F82H and ferritic alloys // *J. Nucl. Mater*. 2019, v. 515, p. 294-302.

77. H. Kishimoto, K. Yutani, R. Kasada, A. Kimura. Helium cavity formation research on oxide dispersed strengthening (ODS) ferritic steels utilizing dual-ion irradiation facility // *Fusion Eng. Des*. 2006, v. 81, p. 1045-1049.

78. R. Schaublin, Y.L. Chiu. Effect of helium on irradiation-induced hardening of iron: a simulation point of view // *J. Nucl. Mater*. 2007, v. 362, p. 152-160.

79. L.K. Mansur. Theory and experimental background on dimensional changes in irradiated alloys // *J. Nucl. Mater*. 1994, v. 216, p. 97-123.

80. A.D. Brailsford, R. Bullough. The rate theory of swelling due to void growth in irradiated metals // *J. Nucl. Mater.* 1972, v. 44, p. 121-135.

81. S.J. Zinkle and L.L. Snead. Designing Radiation Resistance in Materials for Fusion Energy // *Annu. Rev. Mater. Res.* 2014, v. 44, p. 241-267.

82. V.N. Voyevodin, S.A. Karpov, G.D. Tolstolutskaya, M.A. Tikhonovsky, A.N. Velikodnyi, I.E. Kopanets, G.N. Tolmachova, A.S. Kalchenko, R.L. Vasilenko, I.V. Kolodiy. Effect of irradiation on microstructure and hardening of Cr–Fe–Ni–Mn high-entropy alloy and its strengthened version // *Phil. Mag.* 2020, v. 100, N 7, p. 822-836.

83. G.D. Tolstolutska, M.A. Tikhonovsky, S.O. Karpov, V.K. Karpach. Hardening behavior of advanced structural alloys under ion irradiation // *PAST*. 2024. N 2(150), p. 20-27.

84. Liyuan Liu, Yang Zhang, Jihong Han, Xiyu Wang, Wenqing Jiang, Chain-Tsuan Liu, Zhongwu Zhang, and Peter K. Liaw. Nanoprecipitate-Strengthened High-Entropy Alloys // *Advanced Science*. 2021, v. 8, p. 2100870.

85. S.J. Zinkle, Y. Matsukawa. Observation and analysis of defect cluster production and interactions with dislocations // *J. Nucl. Mater*. (Part A). 2004, v. 329-333, p. 88-96.

86. E. Orowan. *Internal Stresses in Metals and Alloys.* Institute of Metals, London, 1948, p. 451.

87. M. Sadeghilaridjani, A. Ayyagari, S. Muskeri, V. Hasannaeimi, R. Salloom, W.-Y. Chen, S. Mukherjee. Ion irradiation response and mechanical behavior of reduced activity high entropy alloy // *J. Nucl. Mater.* 2020, v. 529, p. 151955.

88. G. Velis, M.W. Ullah, H. Xue, K. Jin, M.L. Crespillo, H. Bei, W.J. Weber, Y. Zhang. Irradiation-induced damage evolution in concentrated Ni-based alloys // *Acta Mater.* 2017, v. 135, p. 54-60.

89. Z. Cheng, J. Sun, X. Gao, et al. Irradiation effects in high-entropy alloys and their applications // *J. Alloy. and Compounds.* 2023, v. 930, p. 166768.

90. V.M. Azhazha, O.V. Chernyi, G.E. Storozhilov, N.F. Andrievskaya, T.Yu. Rudicheva. Strained state of Nb-Ti alloy after multidirectional treatment // *PAST*. 2004, N 6(14), p. 136-139.

91. V.N. Voyevodin, G.D. Tolstolutskaya, S.A. Karpov, M.A. Tikhonovsky, G.N. Tolmachova, A.S. Kalchenko, R.L. Vasilenko, I.E. Kopanets. Effect of argon ion irradiation on hardening and microstructure of ferritic-martensitic steel T91 // *PAST.* 2019, N 2(120), p. 7-12.

92. V. Voyevodin, M. Tikhonovsky, G. Tolstolutska, H. Rostova, R. Vasilenko, O. Kalchenko, N. Andrievska, O. Velikodnyi. Structural features and operational characteristics of steel T91 // *East Eur. J. Phys.* 2020, v. 3, p. 93-98.

93. V.N. Voyevodin, G.D. Tolstolutskaya, S.A. Karpov, A.N. Velikodnyi, M.A. Tikhonovsky, A.S. Kalchenko, G.N. Tolmachova, R.L. Vasilenko, I.E. Kopanets. Effect of severe plastic deformation on radiation

hardening of T91 ferritic-martensitic steel // *PAST.* 2021, N 2(132), p. 35-42

94. P. Hosemann, C. Vieh, R.R. Greco, S. Kabra, J.A. Valdez, M.J. Cappiello, S.A. Maloy. Nano-indentation of ion irradiated steels // *J. Nucl. Mater.* 2009, v. 389, p. 239-247.

95. Y. Katoh, M. Ando, A. Kohyama. Radiation and helium effects on microstructures, nano-indentation properties and deformation behavior in ferrous alloys // *J. Nucl. Mater.* 2003, v. 323, p. 251-262.

96. C. Heintze, C. Recknagel, F. Bergner, M. Hernandez-Mayoral, A. Kolitsch. Ion irradiation-induced damage of steels characterized by means of nanoindentation // *Nucl. Instrum. Methods in Phys. Res B*. 2009, v. 267, p. 1505-1508.

97. S. Li, Y. Wang, X. Dai, F. Liu, J. Li, X. Wang. Evaluation of hardening behaviors in ion-irradiated Fe-9Cr and Fe-20Cr alloys by nanoindentation technique // *J. Nucl. Mater*. 2016, v. 478, p. 50-55.

98. B. Li et al. Evaluation of helium effect on irradiation hardening in F82H, ODS, SIMP and T91 steels by nano-indentation method // *Fusion Engineering and Design.* 2019, v. 142, p. 6-12.

99. E.A. Little, R. Bullough, M.H. Wood. On the swelling resistance of ferritic steel // *Proc. R. Soc. Lond. A Math. Phys. Sci*. 1997, v. 372, p. 565-579.

100. R.C. Pasianot, A.M. Monti, G. Simonelli, E.J. Savino. Computer simulation of SIA migration in bcc and hcp metals // *J. Nucl. Mater*. 2000, v. 276, p. 230-234.

101. N. Hashimoto, S. Sakuraya, J. Tanimoto, S. Ohnuki. Effect of impurities on vacancy migration energy in Fe-based alloys // *J. Nucl. Mater*. 2014, v. 445, p. 224-226.

Article received 06.08.2024

ЗМІЦНЕННЯ ЯДЕРНИХ КОНСТРУКЦІЙНИХ МАТЕРІАЛІВ ПРИ ІОННОМУ ОПРОМІНЕННІ

С.О. Карпов, М.О. Азарєнков, Г.Д. Толстолуцька

Оцінка радіаційного зміцнення й окрихчування має критичне значення для розроблення ядерних конструкційних матеріалів нового покоління, стійких до нейтронного опромінення. У цьому огляді узагальнено результати експериментальних спостережень, спрямованих на з'ясування механізмів радіаційно-індукованого зміцнення матеріалів, підданих іонному опроміненню, з акцентом на кореляцію між ефектами опромінення і змінами механічних властивостей. Представлено основні відомості про застосування методів іонного опромінення та наноіндентування для визначення механічних властивостей ядерних конструкційних матеріалів. Проаналізовано вплив опромінення на сучасні конструкційні матеріали, включно з аустенітними сталями, модифікованими ДЗО, феритно-мартенситними сталями та високоентропійними сплавами. Досліджено залежність параметрів зміцнення від дози опромінення та їх зв'язок з мікроструктурною еволюцією. Отримані результати свідчать про те, що ці сучасні сплави демонструють меншу схильність до зміцнення, викликаного опроміненням, порівняно зі звичайними аустенітними нержавіючими сталями.